Title

Macrophage LRRK2 hyperactivity impairs autophagy and induces Paneth cell dysfunction.

Journal

Science Immunology, 9(101)

Authors

Sun, Shengxiang
Hodel, Miki
Wang, Xiang
et al.

Publication Date

2024-11-08

DOI

10.1126/sciimmunol.adi7907

Peer reviewed

HHS Public Access

Author manuscript

Sci Immunol. Author manuscript; available in PMC 2025 January 14.

Published in final edited form as:

Sci Immunol. 2024 November 08; 9(101): eadi7907. doi:10.1126/sciimmunol.adi7907.

Macrophage LRRK2 hyperactivity impairs autophagy and induces Paneth cell dysfunction

Shengxiang Sun[1], **Miki Hodel**[1], **Xiang Wang**[2], **Javier De Vicente**[2], **Talin Haritunians**[3], **Anketse Debebe**[4], **Chen-Ting Hung**[1], **Changqing Ma**[1], **Atika Malique**[1], **Hoang N. Nguyen**[2], **Maayan Agam**[2], **Michael T. Maloney**[2], **Marisa S. Goo**[2], **Jillian H. Kluss**[2], **Richa Mishra**[1], **Jennifer Frein**[1], **Amanda Foster**[1], **Samuel Ballentine**[1], **Uday Pandey**[1], **Justin Kern**[1], **Shaohong Yang**[3], **Emebet Mengesha**[3], **Iyshwarya Balasubramanian**[5], **Annie Arguello**[2], **Anthony A. Estrada**[2], **Nan Gao**[5], **Inga Peter**[4], **Dermot P. B. McGovern**[3], **Anastasia G. Henry**[2], **Thaddeus S. Stappenbeck**[6], **Ta-Chiang Liu**[1,*]

[1]Department of Pathology and Immunology, Washington University School of Medicine, St. Louis, MO 63110, USA.

[2]Denali Therapeutics, South San Francisco, CA 94080, USA.

[3]F. Widjaja Foundation Inflammatory Bowel Disease Institute, Cedars-Sinai Medical Center, Los Angeles, CA 90048, USA.

[4]Department of Genetics and Genomic Sciences, Icahn School of Medicine at Mount-Sinai, New York, NY 10029, USA.

[5]Department of Biological Sciences, Rutgers, State University of New Jersey, Newark, NJ 07102, USA.

[6]Department of Inflammation and Immunity, Cleveland Clinic Lerner Research Institute, Cleveland, OH 44195, USA.

Abstract

LRRK2 polymorphisms (G2019S/N2081D) that increase susceptibility to Parkinson's disease and Crohn's disease (CD) lead to LRRK2 kinase hyperactivity and suppress autophagy. This connection suggests that LRRK2 kinase inhibition, a therapeutic strategy being explored for Parkinson's disease, may also benefit patients with CD. Paneth cell homeostasis is tightly regulated by autophagy, and their dysfunction is a precursor to gut inflammation in CD. Here, we found that patients with CD and mice carrying hyperactive *LRRK2* polymorphisms developed Paneth cell dysfunction. We also found that LRRK2 kinase can be activated in the context

*Corresponding author: ta-chiang.liu@wustl.edu.

Author contributions: S.S. and T.-C.L. wrote the manuscript and designed the experiments. S.S., M.H., C.-T.H., A.M., H.N.N., M.A., M.T.M., M.S.G., J.H.K., R.M., J.F., A.F., U.P., J.K., I.B., A.A., A.A.E., A.G.H., and T.-C.L. conducted experiments and acquired data. T.H., A.D., S.B., S.Y., E.M., and D.P.B.M. provided samples. S.S., X.W., J.D.V., C.-T.H., and T.-C.L. analyzed data. S.S., X.W., N.G., and T.-C.L. interpreted data. S.S., T.-C.L., X.W., C.M., N.G., I.P., and T.S.S. reviewed and edited the manuscript. All authors approved the final manuscript.

Competing interests: J.D.V. and A.A.E. have a patent application (WO2017218843) that includes DN-9713. D.P.B.M. owns stock in Prometheus Biosciences Inc. D.P.B.M. has consulted for Gilead, Pfizer, Boehringer Ingelheim, Qu Biologics, Bridge Biotherapeutics, Takeda, and Palatin Technologies, and received grant support from Janssen. T.S.S. consulted for Janssen, Abbvie, and Nxera. T.-C.L. has research contracts with Denali and Interline Therapeutics. All other authors declare that they have no competing interests.

of interactions between genes (genetic autophagy deficiency) and the environment (cigarette smoking). Unexpectedly, lamina propria immune cells were the main intestinal cell types that express LRRK2, instead of Paneth cells as previously suggested. We showed that LRRK2-mediated pro-inflammatory cytokine release from phagocytes impaired Paneth cell function, which was rescued by LRRK2 kinase inhibition through activation of autophagy. Together, these data suggest that LRRK2 kinase inhibitors maintain Paneth cell homeostasis by restoring autophagy and may represent a therapeutic strategy for CD.

INTRODUCTION

Innate immunity plays an important role in gut homeostasis (1). Within the small intestine, several intestinal epithelial cell types have secretory functions to modulate innate immunity (2). Goblet cells secrete mucin to provide a mucosal barrier, whereas Paneth cells secrete antimicrobial peptides (e.g., defensins and lysozymes) (3). Dysfunction of goblet and Paneth cells is linked to multiple gut inflammatory disorders, including inflammatory bowel disease (IBD) (4). Paneth cells are predominantly located in the small intestine with the highest density in terminal ileum, where Crohn's disease (CD; one of the two main IBD subtypes) is commonly found (2). Paneth cells also have the distinct function of providing niche factors for the nearby intestinal stem cells (5). Given their dual roles in regulating gut immunity and stem cell homeostasis, it has been postulated that Paneth cells are the origin of intestinal inflammation (2).

Recent advances in IBD pathogenesis research have shown that both genetics and environmental risk factors interact and trigger gut inflammation in these patients (4). Genome-wide association studies have identified >200 susceptibility loci for CD (6). Multiple environmental factors that increase CD susceptibility or severity have been identified (7). Among the known CD susceptibility genes, several (including *ATG16L1*, *IRGM*, and *NOD2*) are critical players in the autophagy pathway, and single-nucleotide polymorphisms (SNPs) associated with these genes also result in autophagy defects (8). Therefore, autophagy dysfunction could drive CD development. We previously showed that patients with CD harboring *ATG16L1* or *NOD2* variants are prone to develop Paneth cell morphology defects, a widely used surrogate readout for Paneth cell function (9). We further showed that the Paneth cell phenotype is a cellular biomarker that can integrate the impact of both host genetics and environmental factors (10). As an example, patients with CD and mice harboring *ATG16L1* T300A that are exposed to cigarette smoking are more likely to develop an abnormal Paneth cell phenotype (11). Clinically, an abnormal Paneth cell phenotype correlates with mucosal dysbiosis in CD (12) and a more aggressive disease outcome in CD (11). Therefore, Paneth cell phenotype is biologically and clinically relevant to CD and can be used to dissect potential pathogenic risk factors.

In addition to *ATG16L1* and *NOD2*, the recently identified CD susceptibility gene *leucine-rich repeat kinase 2* (*LRRK2*) also regulates autophagy, with increased LRRK2 kinase activity impairing autophagy (13). *LRRK2* encodes a large protein including a serine/threonine protein kinase domain (14). Several *LRRK2* SNPs that lead to LRRK2 hyperactivity were identified as Parkinson's disease susceptibility loci (15) and were also

found to increase CD susceptibility (16). Transgenic mice overexpressing *Lrrk2* develop more severe dextran sodium sulfate–induced colitis, with LRRK2 hyperactivity causing inactivation of Beclin1, an upstream regulator that induces autophagy, resulting in autophagy inhibition (13). A previous study showed that LRRK2 modulates lysozyme sorting in Paneth cells (17). However, the mechanisms by which LRRK2 activity regulates Paneth cell function, whether autophagy is relevant for LRRK2-dependent Paneth cell function, and whether hyperactive LRRK2 and defective autophagy represent a common driver for Paneth cell dysfunction critical to CD pathogenesis remain unclear.

Here, we showed that patients with CD with *LRRK2* N2081D or G2019S SNPs were prone to harbor Paneth cell defects. In mice, LRRK2 kinase hyperactivity could be triggered by harboring either *Lrrk2* G2019S or other gene-environment interactions such as *Atg16l1* T300A–smoking (11). We also observed that LRRK2 is predominantly expressed in the lamina propria phagocytes, rather than Paneth cells or other intestinal epithelial cells as previously suggested (17). As a proof of concept, we showed that cigarette smoke condensate (CSC)–treated bone marrow–derived macrophages (BMDMs) from *Atg16l1* T300A mice induced LRRK2 kinase hyperactivity, leading to increased secretion of tumor necrosis factor–α (TNFα) and PAI-1, which led to Paneth cell defects in a non-Paneth cell autonomous fashion. Last, we found that this process can be reversed by either LRRK2 inhibition or autophagy activation through Beclin1. Therefore, restoring the LRRK2-Beclin1 balance represents a potential therapeutic strategy to maintain gut innate immunity in CD.

RESULTS

Patients with CD and mice harboring *LRRK2* risk alleles develop Paneth cell defects

We previously showed that the *LRRK2* M2397T SNP is associated with Paneth cell defects in Japanese patients with CD but not North American patients with CD (18). Unlike the *LRRK2* N2018D and G2019S SNPs that are both located within the LRRK2 kinase domain and induce LRRK2 kinase hyperactivity (16), M2397T is not located within the LRRK2 kinase domain (19) and thus is not expected to enhance LRRK2 kinase activity (19). Here, we analyzed Paneth cell numbers and morphology from small intestinal tissue sections of 382 North American patients with CD previously genotyped for *LRRK2* N2018D or G2019S SNPs, which induce LRRK2 kinase hyperactivity (table S1). We found that patients harboring either N2081D or G2019S (all were heterozygous) had fewer ileal Paneth cells/crypt (Fig. 1A) and lower percentages of normal Paneth cells [as a surrogate for Paneth cell function (9, 11) and assessed by human defensin 5] compared with those who did not carry these risk alleles [designated as “nonrisk (NR)”]. The abnormal Paneth cell subtypes included diminished (D2), diffuse (D3), and excluded (D4) (Fig. 1, B and C). We next analyzed mice with a homozygous knock-in (KI) allele that was analogous to the *Lrrk2* G2019S SNP (13). Mice homozygous for this SNP also showed reduced ileal Paneth cells (Fig. 1D) and percentages of normal Paneth cells (Fig. 1E). Therefore, both patients with CD and mice harboring *LRRK2* risk SNPs can have Paneth cell defects.

LRRK2 kinase inhibitor rescues Paneth cell defects in *Lrrk2* G2019S mice

We had previously shown that crypt base apoptosis (rather than necroptosis) was key to Paneth cell defects in patients with CD and mice harboring the *ATG16L1* T300A risk allele and exposed to cigarette smoking (11), and cell death plays roles in intestinal homeostasis (20–22). To further test whether elevated LRRK2 activity causes Paneth cell defects and apoptosis, we treated *Lrrk2* G2019S mice with the LRRK2 inhibitor DN-9713 (Fig. 1F, figs. S1 to S3, and tables S2 to S6). DN-9713 can be administered through diet formulation to mice over several weeks with consistent coverage of IC_{50}-IC_{90} (as assessed by measurement of unbound plasma levels) (fig. S4 and tables S7 and S8). DN-9713 inhibited LRRK2 kinase activity in both human peripheral blood mononuclear cells (PBMCs) and human embryonic kidney (HEK) 293T cells expressing *LRRK2* G2019S (Fig. 1, G and H). Further, DN-9713 showed acceptable in vivo pharmacokinetics and pharmacodynamics profiles (fig. S4). We dosed *Lrrk2* G2019S and wild-type (WT) littermates with either vehicle or DN-9713 in the diet for 2 weeks. Both pharmacokinetics analysis (measured by DN-9713 unbound concentration) and LRRK2 kinase activity (measured by pS935 LRRK2 and pT73 RAB10) demonstrated LRRK2 kinase inhibition (Fig. 1, I and J). *Lrrk2* G2019S mice showed decreased percentages of normal Paneth cells and excessive apoptosis in ileal crypts compared with WT controls, which were prevented by DN-9713 (Fig. 1, K to M).

LRRK2 expression is detected in lamina propria phagocytes but not intestinal epithelial cells

To identify the cell type(s) that express detectable *LRRK2*, we performed in situ hybridization of *Lrrk2* and immunohistochemistry (IHC) of LRRK2 in ilea from mice and patients with CD. We observed detectable *Lrrk2* mRNA expression in murine lamina propria mononuclear cells and not epithelial cells (Fig. 2A). We confirmed that ileal sections of $Lrrk2^{-/-}$ (*Lrrk2* knockout) mice showed no detectable *Lrrk2* mRNA staining in any cells (Fig. 2B). Using multiple LRRK2 antibodies that are used for IHC or immunofluorescence, we observed nonspecific IHC staining in the WT and $LRRK2^{-/-}$ human cells (fig. S5A) and in lamina propria cells from WT and $Lrrk2^{-/-}$ intestinal sections (fig. S5, B to D), despite an immunoblot showing a lack of LRRK2 expression in the human $LRRK2^{-/-}$ cells (fig. S5E) and in the BMDMs from $Lrrk2^{-/-}$ mice (fig. S5F). Despite these caveats, LRRK2 expression was not detected in the intestinal epithelial cells in human or mouse ileum samples (Fig. 2C and fig. S5, B to D and G). Because it has been reported that Paneth cells may express LRRK2 (17), we explored additional approaches to address this discrepancy. An analysis of previously published mouse intestinal epithelial cell single-cell RNA sequencing (scRNA-seq) datasets showed no detectable *Lrrk2* transcripts in epithelial cells (Fig. 2D and fig. S6A) (23, 24). We also isolated Paneth cells from a Paneth cell reporter mouse strain ($Lyz1^{3'UTRCreER}$; *Rosa26R-tdT*) (25) and were unable to detect *Lrrk2* transcripts by scRNA-seq (fig. S6B) (25). These studies support our model that all intestinal epithelial lineages including Paneth cells have either no or low levels of *Lrrk2* expression. In contrast, the scRNA-seq datasets on human intestinal myeloid and human immune cells showed robust *LRRK2* expression in macrophages (Fig. 2E) (26) and classical monocytes (fig. S6C) (27).

To further confirm these findings, we performed immunoblots on WT murine BMDMs and ileal organoids. We were able to detect LRRK2 expression only in BMDMs but not in ileal organoids (Fig. 2, F and G). Likewise, performing in situ hybridization of *Lrrk2*, we found that BMDMs showed robust *Lrrk2* expression (Fig. 2H), whereas it was not detectable in ileal organoids (Fig. 2I). Together, these results show that LRRK2 is mainly expressed in lamina propria myeloid-derived cells and not in intestinal epithelial cells. Our findings also suggest that phagocytes with high LRRK2 activity lead to Paneth cell defects in *Lrrk2* G2019S mice and may act in a non–cell-autonomous fashion.

LRRK2 kinase inhibitor rescues Paneth cell defects in *Atg16l1* T300A smoke-exposed mice

We previously showed that mice harboring the CD risk allele *Atg16l1* T300A developed Paneth cell defects after exposure to cigarette smoke, which are mediated by TNFα-induced crypt base apoptosis (11). We hypothesized that LRRK2 kinase hyperactivity also drives Paneth cell defects in *Atg16l1* T300A smoke-exposed mice. In support of this hypothesis, compared with the control mice, whole ileal lysates from *Atg16l1* T300A smoke-exposed mice showed increased pS106 RAB12, a readout for LRRK2 kinase activity (28) (Fig. 3A). Of note, we also performed IHC on samples from *Atg16l1* T300A smoke-exposed mice and found no LRRK2 expression in Paneth cells (fig. S7A). We next tested whether LRRK2 kinase inhibition rescues smoking-induced Paneth cell defects in *Atg16l1* T300A mice by exposing them to cigarette smoke and dosing them with vehicle or DN-9713 in the diet for 2 weeks (Fig. 3B). Similar to *Lrrk2* G2019S mice, LRRK2 kinase inhibition was achieved, as measured by both pharmacokinetic and pS935 LRRK2 analysis (fig. S7, B and C). DN-9713 treatment decreased pT73 RAB10 (fig. S7D) and rescued ileal Paneth cell defects and numbers of crypt base cleaved caspase 3 $(CC3)^+$ cells in *Atg16l1* T300A smoke-exposed mice (Fig. 3, C and D). To further confirm the role of LRRK2 in mediating Paneth cell defects, we evaluated the impact of *Lrrk2* deletion by crossing the *Atg16l1* T300A to $Lrrk2^{-/-}$ mice. As expected, *Atg16l1* T300A/$Lrrk2^{-/-}$ mice were also protected from smoking-induced Paneth cell defects (Fig. 3E) and crypt base apoptosis (Fig. 3F). Together, both pharmacological kinase inhibition of LRRK2 and *Lrrk2* deletion prevented smoking-induced Paneth cell defects in *Atg16l1* T300A mice, suggesting that LRRK2 activity may mediate the Paneth cell defects in *Atg16l1* T300A mice exposed to cigarette smoke, like *Lrrk2* G2019S mice.

Atg16l1 T300A macrophages secrete factors to induce Paneth cell defects in organoids

We next hypothesized that intestinal myeloid-derived cells are the key cell types that mediate smoking-induced Paneth cell defects in *Atg16l1* T300A mice. We depleted myeloid-derived cells using intravenous injection of clodronate liposomes or a colony-stimulating factor 1 receptor (CSF1R) blocking antibody (fig. S8, A and B). Both treatments prevented Paneth cell defects and crypt base apoptosis in *Atg16l1* T300A smoke-exposed mice (Fig. 4, A to D) and *Lrrk2* G2019S mice (Fig. 4, E and F). To determine the mechanism(s) by which LRRK2 in macrophages modulates Paneth cells, we used BMDMs and ileal organoids to assess the interaction between macrophages and Paneth cells. *Atg16l1* T300A or WT BMDMs were treated with CSC with or without polyinosinic-polycytidylic acid [poly(I:C) (29)], and LRRK2 kinase activity was assessed by measuring pS106 RAB12 via immunoblotting (Fig. 4G and fig. S9, A and B) and pT73 RAB10 by flow cytometry

[using protocol described in (30, 31)] (fig. S9, C and D). The expression of pS106 RAB12 and pT73 RAB10 in untreated, CSC-treated, or poly(I:C)–treated BMDMs was comparable between the *Atg16l1* T300A and WT groups (fig. S9, A to D). When BMDMs were treated with CSC in conjunction with poly(I:C), WT BMDMs showed lower LRRK2 kinase activity compared with *Atg16l1* T300A BMDMs (Fig. 4, G and H, and fig. S9, A to D). Notably, DN-9713 reduced LRRK2 kinase activity (pS106 RAB12) in both *Atg16l1* T300A and WT BMDMs treated with CSC + poly(I:C) (Fig. 4, G and H).

We next tested whether direct macrophage-Paneth cell contact was required to trigger Paneth cell defects. We transferred BMDM medium to ileal organoids and measured Paneth cell densities in the culture in three subsequent experiments (Fig. 4I). First, we assessed whether *Atg16l1* T300A–CSC interactions in BMDMs affect Paneth cell density in organoids. We found that whereas WT organoids did not show changes in the Paneth cell densities when treated with medium from WT BMDMs/CSC + poly(I:C), there was a reduction in Paneth cell density when organoids were treated with medium from *Atg16l1* T300A BMDMs/CSC + poly(I:C) (Fig. 4, J to L), suggesting that the *Atg16l1* T300A mutation in macrophages contributes to the observed Paneth cell defects. Robust Paneth cell loss and increased $CC3^+$ cells were observed in the *Atg16l1* T300A organoids when treated with medium from *Atg16l1* T300A BMDMs/CSC + poly(I:C) (Fig. 4, J to L). We also performed immunofluorescence in *Atg16l1* T300A organoids treated with medium from *Atg16l1* T300A BMDMs/CSC + poly(I:C) but did not identify colocalization of lysozyme and CC3 (fig. S10). This suggests either that Paneth cell loss in *Atg16l1* T300A organoids may not be due to death of Paneth cells themselves or that lost Paneth cells were not captured in our staining. We next assessed the effect of LRRK2 inhibition on the interaction of macrophages and Paneth cells using DN-9713 or BMDMs from *Atg16l1* T300A/$Lrrk2^{-/-}$ mice. *Atg16l1* T300A organoids cultured with medium from either *Atg16l1* T300A BMDMs/CSC + poly(I:C) treated with DN-9713 or *Atg16l1* T300A/$Lrrk2^{-/-}$ BMDMs/CSC + poly(I:C) showed rescue of Paneth cell density and cell death (Fig. 4, M to O). To further test the importance of macrophage-expressed *Lrrk2*, we generated *Lrrk2* myeloid conditional knockout mice ($Lrrk2^{\Delta phg}$ strain; generated using $LysM^{Cre}$) and further crossed this strain with the *Atg16l1* T300A mice to generate *Atg16l1* T300A/$Lrrk2^{\Delta phg}$ mice. *Atg16l1* T300A/$Lrrk2^{\Delta phg}$ mice were protected from smoking-induced Paneth cell defects and crypt base $CC3^+$ cells (Fig. 4, P and Q). Last, we found that medium from *Lrrk2* G2019S BMDMs/poly(I:C) decreased Paneth cell density and increased apoptosis in WT organoids (Fig. 4, R to T). In sum, these data support the hypothesis that macrophage LRRK2 kinase hyperactivity triggers Paneth cell defects without the need for cell-cell contact.

TNF and PAI-1 secreted by *Atg16l1* T300A macrophages mediate Paneth cell defects

Because we observed that cell-cell contact was not required for macrophage-induced Paneth cell defects, we sought to identify soluble factors secreted from BMDMs mediating these effects using a multiplex cytokine/chemokine array. Compared with treated WT BMDMs, *Atg16l1* T300A BMDMs/CSC + poly(I:C) showed increased production of a wide variety of cytokines and chemokines, including CCL6, MCP-5, CXCL12, IL-27, MCP-1, PAI-1, TNFα, CXCL16, IL1F3, CCL3, and osteopontin (Fig. 5A and fig. S11A). We validated

the enhanced expression of CCL6, MCP-5, CXCL12, IL-27, MCP-1, PAI-1 and TNFα by enzyme-linked immunosorbent assay (ELISA) (Fig. 5, B and C, and fig. S11, B to L). DN-9713 significantly reduced the production of most of these cytokines and chemokines (Fig. 5, A to C, and fig. S11, A to L). An analysis of an scRNA-seq intestinal epithelial cell dataset (23) showed undetectable expression of receptors for MCP-5, MCP-1, CXCL12, CCL6, and IL-27 (fig. S12, A to E). We validated this finding by performing quantitative polymerase chain reaction (fig. S12F) and immunoblotting of TNFα and PAI-1 receptors (TNFR1 and LRP1, respectively) in WT ileal organoids (Fig. 5D). *Lrrk2* G2019S BMDMs treated with poly(I:C) also showed increased TNFα and PAI-1 (Fig. 5, E and F), and likewise, *Lrrk2* G2019S ilea showed higher TNFα and PAI-1 levels (fig. S13, A and B). Therefore, TNFα and/or PAI-1 likely modulates Paneth cell defects in these models.

We next administered specific inhibitors to TNFα and PAI-1 into organoid cultures (Fig. 5G). An anti-TNFα antibody and the PAI-1 inhibitor MDI-2268 prevented Paneth cell defects and apoptosis in *Atg16l1* T300A organoids (Fig. 5, H to J). Of note, this is consistent with our previous study that showed genetic blockade of TNFα signaling rescues Paneth cell defects in *Atg16l1* T300A smoke-exposed mice (11). We found that the PAI-1 inhibitor prevented Paneth cell defects and crypt base apoptosis from *Atg16l1* T300A smoke-exposed mice (Fig. 5, K and L). We further tested these inhibitors in *Lrrk2* G2019S mice and found that they also rescued Paneth cell defects in *Lrrk2* G2019S mice (Fig. 5, M and N). Lastly, to determine whether *Atg16l1* loss of function in phagocytes alone drives Paneth cell defects, we generated myeloid-specific *Atg16l1* knockout mice ($Atg16l1^{\Delta phg}$; using $LysM^{Cre}$). These mice also developed smoking-induced Paneth cell defects (Fig. 5O), which were rescued by DN-9713 (Fig. 5, P and Q). Together with our previous studies demonstrating $Atg16l1^{\Delta PC}$ (Paneth cell–specific *Atg16l1* knockout using $Defa4^{Cre}$) mice developed smoking-induced Paneth cell defects (11), our findings suggest that the enhanced proinflammatory responses from *Atg16l1*-deficient macrophages contribute to the development of smoking-induced Paneth cell defects, which can be further enhanced by autophagy deficiency in the Paneth cells themselves.

LRRK2-Beclin1 balance modulates Paneth cell defects in mice

Given that *Atg16l1* T300A mice have autophagy defects (32) and LRRK2 has been reported to play an important role in regulating autophagy (13), we hypothesized that LRRK2 mediates Paneth cell defects in *Atg16l1* T300A smoke-exposed mice through regulating autophagy. We found that ilea from *Lrrk2* G2019S mice showed higher p62 induction (an indicator of defective autophagy), and *Atg16l1* T300A non–smoke-exposed mice showed a similar trend (Fig. 6, A and B). LRRK2 interacts with and leads to Beclin1 inactivation (33), thereby inhibiting autophagy (13). Furthermore, *Becn1* (encoding Beclin1)–deficient HCT116 cells showed increased LRRK2 expression (13). These studies suggest a bidirectional relationship between LRRK2 and Beclin1. We therefore postulated that the LRRK2-BECLIN1 balance in macrophages could modulate Paneth cell defects in the context of smoking. We found that *Atg16l1* T300A BMDMs/CSC + poly(I:C) had defective autophagy with higher p62 induction and lower pS15 Beclin1 than WT BMDMs (Fig. 6, C to E). Likewise, *Lrrk2* G2019S BMDMs/poly(I:C) also showed increased p62 and decreased pS15 Beclin1 expression (Fig. 6, F to H). These data suggest that LRRK2-

dependent regulation of Beclin1 and autophagy may be a common mechanism driving Paneth cell dysfunction.

We next hypothesized that proper expression and function of Beclin1 in BMDMs could rescue Paneth cell defects. To test whether Beclin1 activation could restore homeostasis in the context of LRRK2 hyperactivity, we crossed the *Atg16l1* T300A mice to *Becn1* F121A (*Becn1* KI) mice that have constitutively high *Becn1* expression (34). BMDMs from *Atg16l1* T300A and *Atg16l1* T300A/*Becn1* KI mice were used to test the role of Beclin1 on Paneth cell defects (Fig. 6I). *Atg16l1* T300A/*Becn1* KI BMDMs treated with CSC/poly(I:C) did not show increased PAI-1 or TNFα production, in contrast with effects observed in the *Atg16l1* T300A group (Fig. 6, J and K). *Atg16l1* T300A/*Becn1* KI BMDMs treated with CSC/poly(I:C) also showed a trend of decreased production for other cytokines (fig. S14, A to M). In addition, medium transfer from *Atg16l1* T300A/*Becn1* KI BMDMs treated with CSC/poly(I:C) prevented the Paneth cell defects and cell death in *Atg16l1* T300A organoids compared with those that received medium from *Atg16l1* T300A BMDMs (Fig. 6, L to N). Furthermore, *Atg16l1* T300A/*Becn1* KI mice were protected from smoking-induced Paneth cell defects and cell death (Fig. 6, O and P), and a Tat-Beclin1 peptide (35) also showed similar protective effects in *Atg16l1* T300A mice (Fig. 6, Q and R). We further administered Tat-Beclin1 peptide to *Lrrk2* G2019S mice, which rescued both Paneth cell defects and crypt base apoptosis (Fig. 6, S and T). Therefore, increased Beclin1 expression, both pharmacologically and genetically, could prevent Paneth cell defects in *Atg16l1* T300A smoke-exposed mice and *Lrrk2* G2019S mice.

DISCUSSION

Because of the identification of several *LRRK2* SNPs as CD susceptibility alleles, studies have revealed the possible roles of LRRK2 in mediating intestinal inflammation (19). As a result, there is tremendous interest in testing whether LRRK2 kinase inhibitors, currently in Parkinson's disease clinical trials (36), may also benefit patients with CD. Here, we showed that patients with CD with *LRRK2* risk alleles were prone to develop Paneth cell defects. Similarly, *Lrrk2* G2019S mice showed Paneth cell defects. LRRK2 kinase inhibition rescued Paneth cell defects in two mouse models: the *Lrrk2* G2019S and the *Atg16l1* T300A smoke-exposed mice. We also made the unexpected finding that lamina propria immune cells, but not Paneth cells, were the main cell types in the intestine that express LRRK2. Further, *Atg16l1* T300A BMDMs treated with CSC/poly(I:C) had higher LRRK2 activity, resulting in enhanced TNFα and PAI-1 production and Paneth cell defects. Last, we showed that activation of autophagy by overexpressing *Becn1* or Tat-Beclin1 peptide restored LRRK2 hyperactivity-induced proinflammatory responses.

Much of our research strategy for LRRK2 was initially based on previous studies suggesting that Paneth cells express LRRK2 (17). However, multiple scRNA-seq datasets and our data from this study reveal that in the small intestine, LRRK2 is predominantly expressed in phagocytes such as macrophages. Previous scRNA-seq studies suggest that LRRK2 may function in other phagocytes, including monocytes and dendritic cells, further highlighting that LRRK2 likely modulates intestinal epithelium in a non–Paneth cell autonomous fashion.

Another major finding of our work is that LRRK2 hyperactivity can be triggered by either host genetics alone (*LRRK2* risk alleles) or gene-environment interactions (e.g., *Atg16l1* T300A-smoking) that do not involve host *LRRK2* polymorphisms. This has important clinical implications, because it suggests that LRRK2 activity may be a common regulator for gut epithelial innate immunity. In addition, assessing patients' LRRK2 activity status may offer better biological insight than genotyping for *LRRK2* SNPs alone. Given the relatively low prevalence of *LRRK2* risk alleles in CD (compared with other genes such as *ATG16L1*), our data suggest that LRRK2-targeting therapies such as LRRK2 kinase inhibitors may benefit patients with CD with and without *LRRK2* risk alleles. Further development of biomarkers to define the LRRK2 activity status of patients may allow for refinement of clinical studies for CD.

A recent study showed that *Atg16l1* T300A BMDMs exhibit enhanced pro-inflammatory responses upon treatment with Toll-like receptor or NOD (nucleotide-binding and optimization domain)–like receptor stimulation (37). Further, LRRK2 hyperactivity results in the up-regulation of TNFα in Parkinson's disease in the central nervous system (38). Consistent with our findings, *Lrrk2*-overexpressing bone marrow–derived dendritic cells also had higher TNFα expression (13), and *Lrrk2* G2019S mice exhibit increased inflammatory responses and susceptibility to infection (39). These findings highlight that LRRK2 could be a master regulator of inflammatory diseases, modulating pro-inflammatory cytokine/chemokine production from phagocytes. Our working model is that gene/gene-environment interactions lead to LRRK2 hyperactivity in phagocytes, which then secrete proinflammatory factors that ultimately detrimentally affect intestinal epithelial cells (Fig. 6U).

Cigarette smoking is known to increase intracellular reactive oxygen species (ROS) (40), and ATG16L1 plays a role in maintaining intracellular ROS homeostasis in the intestine (20), implying that *Atg16l1* T300A-smoking interactions may enhance oxidative stress. Damaged lysosomal function induces LRRK2 activation in macrophages (41). Given that ROS has been shown to damage the lysosome function (42) and ROS also activates LRRK2 kinase in HEK293 cells (43), we speculate that *Atg16l1* T300A-smoking interaction may activate LRRK2 through impaired lysosomal function.

Our Beclin1 data support previous findings that LRRK2 hyperactivity inhibits autophagy via inactivating Beclin1 (13). Our findings are also consistent with previous studies that linked Beclin1 deficiency to inflammasome activation, which leads to enhanced pro-inflammatory cytokine secretion (44). Our data suggest that homeostasis between LRRK2 and Beclin1 is required to keep inflammation in check (13). We speculate that in the scenario where LRRK2 kinase activity remains high, either blocking LRRK2 activity with inhibitors or enforcing Beclin1 expression could reverse the pro-inflammatory state. Together, these findings suggest a potential yin and yang relationship between LRRK2 and Beclin1 in which offsetting the balance could increase susceptibility to inflammation. Our study also supports the notion that autophagy regulates the homeostasis of gut innate immunity.

Lastly, from a therapeutic perspective, our study provides several potential avenues to target Paneth cell dysfunction. In addition to TNFα- and PAI-1–targeted approaches,

LRRK2 kinase inhibitors may provide additional value by targeting different steps in the molecular pathway. In summary, our study provides mechanistic insight into how a key CD susceptibility gene, *LRRK2,* regulates intestinal epithelial homeostasis. LRRK2-targeting therapies may be beneficial in treating patients with CD harboring *LRRK2* risk alleles and/or with high LRRK2 kinase activity in the gut.

MATERIALS AND METHODS

Study design

The objective of this study was to investigate the effects of LRRK2 in phagocytes on small intestinal Paneth cells. We detected Paneth cell phenotypes in the LRRK2 hyperactivity samples from 382 patients with CD carrying *LRRK2* risk alleles (N2081D and G2019S) and *Lrrk2* G2019S and *Atg16l1* T300A smoke-exposed mice. BMDMs from these mice were used for LRRK2 activity detection. All mouse experiments were performed with random assignment. Interpretation of Paneth cell phenotypes was done in a blinded fashion. All data collected were included for quantification, and no outliers were excluded. At least three biological replicates per experimental group were used.

Mice

*Lrrk2 G*2019S mice were obtained from Taconic (catalog no. 13940). $Lrrk2^{fl/fl}$ mice were obtained from the Jackson Laboratory (catalog no. 024469). *Atg16l1* T300A mice were obtained from R. Xavier (Broad Institute) as described previously (11). $Atg16l1^{\Delta phg}$ mice were generated by crossing $Atg16l1^{fl/fl}$ mice to $LysM^{Cre}$ mice (the Jackson Laboratory, catalog no. 4781). $Lrrk2^{-/-}$ (*Lrrk2* knockout) mice were obtained from the Jackson Laboratory (catalog no. 016121). *Becn1* F121A mice were generously provided by C. He (Northwestern University). *Atg16l1* T300A mice crossed with $Lrrk2^{-/-}$ or *Becn1* F121A mice to generate *Atg16l1* T300A/$Lrrk2^{-/-}$ and *Atg16l1* T300A *Becn1* F121A (T300A/*Becn1* KI) mice. $Lrrk2^{\Delta phg}$ mice were generated by crossing $Lrrk2^{fl/fl}$ to the $LysM^{Cre}$ mice. The $Lrrk2^{\Delta phg}$ mice were subsequently crossed with *Atg16l1* T300A to generate T300A/$Lrrk2^{\Delta phg}$ mice. Paneth cell reporter mice were generated by crossing $Lyz1^{3'UTR\text{-}CreER}$ mice to *Rosa26R-tdTomato* (tdT) reporter mice as previously reported (25). All mice were of the C57BL/6 genetic background and maintained in a specific pathogen–free facility and bred in heterozygotes-to-heterozygotes fashion. All experimental procedures were approved by the Washington University Institutional Animal Care and Use Committee and performed according to the ARRIVE guidelines.

Cigarette smoking model

Six- to eight-week-old mice were exposed to cigarette smoke for 2 weeks to trigger Paneth cell defects as previously described (11).

Phagocyte depletion

For clodronate, 40 μl from 23 mg/ml stock (Encapsula Nano Sciences) was mixed with 160 μl of molecular-grade phosphate-buffered saline (PBS) (45). Mice were then injected with clodronate or control liposomes intraperitoneally twice per week for 2 weeks. For the CSF1R experiment, mice were treated intraperitoneally with anti-CSF1R antibody or

immunoglobulin G2a (IgG2a) isotype control antibody, at 700 μg per mouse on day 0 and 300 μg per mouse every other day for 2 weeks.

Inhibition of TNFα and PAI-1 in mice

Mice were treated intraperitoneally with anti-TNFα antibody with a dose of 0.5 mg per mouse per injection (two injections per week), IgG1 control antibody for 2 weeks (11), or PAI-1 inhibitor MDI-2268 with a dose of 73 μg per mouse every day for 2 weeks.

Paneth cell phenotype analysis

Lysozyme (1:100; Santa Cruz, catalog no. sc-27958) and human defensin 5 (1:2000; NovusCat, catalog no. NB110–60002) were used for immunofluorescence. For both human and mouse samples, each Paneth cell was classified into normal (D0) or one of the five abnormal (D1 to D5) categories, including D1, disordered (abnormal distribution and size of the granules); D2, diminished (≤10 granules); D3, diffuse (smear of lysozyme or defensin within the cytoplasm with no recognizable granules); D4, excluded (majority of the granules do not contain stainable material); and D5, enlarged (rare, mega granules). At least 40 to 100 crypts were quantified for each sample because we have previously shown that a minimum of 40 crypts is required to adequately define Paneth cell phenotype.

LRRK2 inhibitor treatment in mice

DN-9713 was used as a peripherally restricted LRRK2 kinase inhibitor for in vivo studies. Grain-based, bacon-flavored rodent chow was formulated into pellets containing DN-9713 (0.0025% or 2.5 g of DN-9713 per kilogram of diet, estimated to be 250 mg/kg per animal per day) and irradiated for in-diet dosing (Bio-Serv; LabDiet; PicoLab Mouse Diet 20, 5058). Mice were provided with vehicle or DN-9713 diet ad libitum for 14 days. Food weight and mouse body weight were routinely monitored to evaluate diet consumption and animal health.

Tat-Beclin1 peptide treatment in mice

Mice were treated intraperitoneally with Tat-Beclin1 peptide or Tat-Beclin1 scrambled control at a daily dose of 16 mg/kg for 2 weeks.

BMDM isolation, stimulation, and secretome determination

Bone cells from femurs and tibias of mice were isolated and plated in sterile dishes containing high-glucose Dulbecco's modified Eagle's medium (DMEM; Sigma-Aldrich, catalog no. 6429) with 5% horse serum (Sigma-Aldrich, catalog no. H1270), 10% fetal bovine serum (Sigma-Aldrich, catalog no. F2442), penicillin-streptomycin (Sigma-Aldrich, catalog no. P4333), 10 mM Hepes (Corning, catalog no. 25–060-CI), 1% L-glutamine, 1% sodium pyruvate, and macrophage colony-stimulating factor (BioLegend, catalog no. 576404) at 10 ng/ml. After plating the BMDMs for 24 hours, the cells were washed with sterile PBS, fresh medium was added, and BMDMs were stimulated with CSC (150 μg/ml), poly(I:C) (100 μg/ml), DN-9713 (5 μM), or vehicle (PBS) for the detection of LRRK2 activity and protein expression and were stimulated with CSC (50 μg/ml), poly(I:C) (100 μg/ml), DN-9713 (5 μM), or vehicle (PBS) for the BMDM secretome detection or further

ileal organoid culture. Poly(I:C) is a reagent commonly used for in vitro stimulation of immune cells such as BMDMs (29). Twenty to 24 hours after stimulation, the BMDM medium was centrifuged, and the cell lysate and supernatant were collected. Twenty hours after stimulation, the cell lysate was used for LRRK2 activity and protein expression determination. Twenty-four hours after stimulation, the supernatant was used to detect the BMDM secretome, as well as further ileal organoid culture. The BMDM secretome was first detected by using the Proteome Profiler Mouse XL Cytokine Array and following the vendor's instructions. The dot intensities for proteome profiling were detected and analyzed by ImageJ. The quantity of selected cytokines and chemokines was further validated by ELISA following the vendors' instructions.

Organoid culture

Intestinal stem cells were cultured in Matrigel (Thermo Fisher Scientific, catalog no. CB-40234) and medium with 50% L-WRN conditioned medium. Organoids were passaged mechanically from stem cells and seeded in 24-well plates, then cultured by using EGF/Noggin/R-spondin (ENR) medium. For the BMDM medium transfer experiment, 15% of the total organoid culture volume was from supernatant from various BMDM treatments [including CSC ± Poly(I:C), DN-9713, or PBS] from day 0 to day 3. For a subset of experiments, organoids were also treated with the following: anti-TNF antibody (40 μg/ml) or PAI-1 inhibitor MDI-2268 (1 mM). The medium for spheroid and organoid culture was changed every 2 days. The organoids were then harvested for various assays.

Ileal crypts were cultured in Matrigel in the presence of 50% L-WRN conditioned medium (contains WNT3A, R-Spondin 3, and Noggin). This protocol allows for rapid expansion of intestinal epithelial spheroids enriched with stem cells. The spheroids were plated out on day 0. From day 1 to day 3, the culture cells were cultured in ENR medium, which contains EGF, Noggin, and R-Spondin 1, to allow for Paneth cell differentiation. The organoids were then cultured with 15% medium from the supernatant collected from the BMDM, harvested on day 3, and processed for immunofluorescence.

Bioanalytical analysis of intestine and plasma samples from mice treated with DN-9713

Intestinal and plasma samples were collected from mice for measurement of DN-9713 concentration. Plasma samples were prepared from blood collected into tubes containing K2EDTA as the anticoagulant, and intestinal samples were snap frozen; all samples were stored at −80°C until analysis. Plasma and intestinal DN-9713 concentrations were measured at Quintara Laboratories (Worcester, MA) using a sensitive and selective liquid chromatographic–tandem mass spectrometric (LC-MS/MS) method.

Meso Scale Discovery–based analysis of pT73 RAB10, total LRRK2, and pS935 LRRK2

Capture antibodies were biotinylated using EZ-Link NHS-LC-LC-Biotin (Thermo Fisher Scientific, catalog no. 21343), and detection antibodies were conjugated using Sulfo-TAG NHS-Ester [Meso Scale Discovery (MSD), Rockville, MD, catalog no. R31AA-1]. Ninety-six–well MSD GOLD Small Spot Streptavidin plates (MSD, catalog no. L45SSA-1) were coated with 25 μl of capture antibodies [pS935 LRRK2 (0.5 mg/ml), Abcam, catalog no. ab133450; total LRRK2 (0.5 mg/ml), BioLegend, catalog no. 844401; pT73 RAB10 (1

mg/ml), Denali, catalog no. 19–4] diluted in Diluent 100 (MSD, catalog no. R50AA-2) for 1 hour at room temperature with 700 rpm shaking. After three washes with TBST, 25-μl samples were added to each well and incubated at 4°C overnight with agitation at 700 rpm. After three additional washes with TBST, 25 μl of detection antibodies [total LRRK2 (1 mg/ml), BioLegend, catalog no. 808201; total RAB10 (2 mg/ml), Abcam, catalog no. ab181367] was added to each well diluted in TBST containing 25% MSD blocker A (MSD, catalog no. R93AA-1) together with rabbit (Rockland Immunochemicals, Pottstown, PA, catalog no. D610–1000) and mouse gamma globin fraction (Rockland, catalog no. D609–0100). After a 1-hour incubation at room temperature at 700 rpm and three washes with TBST, 150 μl of MSD read buffer (MSD R92TC, 1:1 diluted with water) was added, and plates were read on the MSD Sector S 600.

In situ hybridization

Ileal tissues from *Lrrk2*$^{-/-}$ and WT mice were pinned out and fixed in 10% neutral buffered formalin overnight at 4°C. BMDMs and ileal organoids were collected and fixed in 4% paraformaldehyde overnight at 4°C. Fixed ileal tissues were washed by using 70% ethanol three times and then blocked in agar to generate a formalin-fixed paraffin-embedded (FFPE) sample. Fixed cell samples were incubated in 20% sucrose (dissolved in PBS) at 4°C for approximately 24 hours and were embedded in optimal cutting temperature (OCT) compound on dry ice and sectioned by a cryostat machine. The unstained frozen slides were washed in PBS to remove the OCT compound and ready for in situ hybridization. Ileal tissues were sectioned, and unstained FFPE slides were baked at 60°C for 1 hour, followed by deparaffinization with xylene and 100% ethanol. The FFPE slides were then brought to room temperature and ready for in situ hybridization. In situ hybridization was performed using a custom-designed Mm-*Lrrk2* probe (ACDBio, catalog no. 1320941-C1), the BaseScope Assay-RED Detection Kit (ACD, catalog no. 323910), RNAScope H_2O_2 & Protease Plus Reagent (ACD, catalog no. 322381), RNAScope Target Retrieval Reagents, and RNAScope Wash Buffer Reagents (ACD, catalog no. 322000) according to the manufacturer's instructions. Sections were then mounted in EcoMount solution (Thermo Fisher Scientific, catalog no. EM897L) and imaged under a microscope.

Immunoblot

Mouse ilea and BMDMs were collected in a lysis buffer of 1× radioimmunoprecipitation assay (RIPA; Sigma-Aldrich, catalog no. R0278) containing protease inhibitor (Sigma-Aldrich, catalog no. P2714–1BTL) and phosphatase inhibitor (Sigma-Aldrich, catalog no. P2850) and centrifuged at 12,000*g* for 12 min at 4°C. Ileal organoids were collected in cell recovery solution (Corning, catalog no. 354253) and centrifuged at 200*g* for 10 min at 4°C. The supernatant was then removed, and RIPA buffer with protease and phosphatase inhibitors was added. Ilea, BMDMs, and ileal organoid lysis solution were put on ice for 30 min for lysing cells. Subsequently, the supernatant was collected to detect protein concentration by the Pierce BCA Protein Assay Kit (Thermo Fisher Scientific, catalog no. 23225) according to the manufacturer's instructions. Sample buffer (5×, Bio-Rad, catalog no. 1610747) was then added to denature protein at 42°C for 1 hour. Proteins were separated by SDS–polyacrylamide gel electrophoresis (Bio-Rad, catalog no. 4561084) and then transferred to a nitrocellulose membrane, which was incubated with primary antibodies

of LRRK2 antibody (1:1000; Abcam, catalog no. ab133474) or LRRK2 antibody (1:1000, Proteintech, catalog no. 75–253-020), pS106 RAB12 (1:500, Abcam, catalog no. ab256487), RAB12 (1:800, Proteintech, catalog no. 18843–1-AP), LRP1 (1:500; CST, catalog no. 64099), TNFR1 (1:800; CST, catalog no. 13377), pS15-Beclin1 (1:500; CST, catalog no. 84966), Beclin1 (1:1000; CST, catalog no. 3738), p62 (1:1000; CST, catalog no. 5114), and glyceraldehyde-3-phosphate dehydrogenase (GAPDH) (1:10,000; CST, catalog no. 2118) for 1 to 3 days at 4°C. After washing with 1× TBST for 45 min, the membrane was incubated in secondary antibodies of goat anti-rabbit or goat anti-mouse (1:10,000; Thermo Fisher Scientific) for 1 hour at room temperature. The densities of target proteins were quantified by Image Studio lite version 5.2 and ImageJ software.

Flow cytometry

Flow cytometry was used to detect pT73 RAB10 and follow the protocol as reported in (30, 31). Briefly, BMDMs were stained with anti-CD45 APC-Cy7 (1:400; 30-F11, BioLegend) and anti-F4/80 Alexa Fluor 488 (1:200; BM8, BioLegend). A LIVE/DEAD fixable aqua dead cell stain kit (1:1000; 50–112-1526, Invitrogen) was used to exclude nonviable cells. After that, cells were fixed and permeabilized overnight using the staining buffer set (00–5523-00, Invitrogen), followed by 1 hour of staining with anti-pT73 RAB10 antibody (1:500, Abcam, catalog no. ab241060) on ice. Subsequently, cells were incubated with PE donkey anti-rabbit IgG (minimal x-reactivity) (1:100; BioLegend, catalog no. 406421) on ice for 1 hour. The fluorescence intensities were measured using a BD LSRFortessa. The data were analyzed using FlowJo.

Statistical analysis

For analysis between two groups, an unpaired nonparametric *t* test or a nonparametric equivalent Mann-Whitney test was used. For analysis between more than two groups, one-way analysis of variance (ANOVA), two-way ANOVA, or nonparametric Kruskal-Wallis test was performed. Nonparametric statistical tests were selected based on the data distribution. All tests were two tailed, and a *P* value of <0.05 was considered significant. Data were plotted and analyzed using GraphPad Prism (version 9.0) and SAS version 9.4 (SAS Institute, Cary, NC). Data represent mean ± SD or mean ± SEM. All statistical details of the experiments can be found in the figure legends, including the statistical tests used and the exact value of *n*.

Supplementary Material

Refer to Web version on PubMed Central for supplementary material.

Acknowledgments:

We thank C. He for providing the *Becn1* F121A mice, M. Swamy for the protocol of pT73 RAB10 flow cytometry, C. Stallings for providing the *Atg16l1*$^{\Delta phg}$ mice, G. Di Paolo for critically reviewing the manuscript, E. Negrou for contributing to the pS935 LRRK2 DRC data in human PBMCs, and R. Takahashi for providing experimental methods.

Funding:

The study was funded by R01 DK125296, DK124274, DK136829 (T.-C.L.), DK 132885 (N.G.), U01 DK062413, Helmsley Charitable Trust (both to D.P.B.M.), and MJFF-021181 (I.P.). The study was also supported in part by the Digestive Disease Research Core Center at Washington University by grant P30 DK052574.

Data and materials availability:

Crystallographic data for this paper have been deposited in the Cambridge Crystallographic Data Centre (www.ccdc.cam.ac.uk/structures) under CCDC number 2390427. Tabulated data underlying the figures are provided in data file S1 and uncropped immunoblots are provided in data file S2. All other data needed to evaluate the conclusions in the paper are present in the paper, the Supplementary Materials, and data file. The LRRK2 inhibitor DN-9713 can be requested from Denali and will be made available upon reasonable request and partner approval through a material transfer agreement.

REFERENCES AND NOTES

1. Thaiss CA, Zmora N, Levy M, Elinav E, The microbiome and innate immunity. Nature 535, 65–74 (2016). [PubMed: 27383981]
2. Adolph TE, Tomczak MF, Niederreiter L, Ko HJ, Böck J, Martinez-Naves E, Glickman JN, Tschurtschenthaler M, Hartwig J, Hosomi S, Flak MB, Cusick JL, Kohno K, Iwawaki T, Billmann-Born S, Raine T, Bharti R, Lucius R, Kweon MN, Marciniak SJ, Choi A, Hagen SJ, Schreiber S, Rosenstiel P, Kaser A, Blumberg RS, Paneth cells as a site of origin for intestinal inflammation. Nature 503, 272–276 (2013). [PubMed: 24089213]
3. Clevers HC, Bevins CL, Paneth cells: Maestros of the small intestinal crypts. Annu. Rev. Physiol. 75, 289–311 (2013). [PubMed: 23398152]
4. Liu TC, Stappenbeck TS, Genetics and pathogenesis of inflammatory bowel disease. Annu. Rev. Pathol. 11, 127–148 (2016). [PubMed: 26907531]
5. Yu S, Tong K, Zhao Y, Balasubramanian I, Yap GS, Ferraris RP, Bonder EM, Verzi MP, Gao N, Paneth cell multipotency induced by notch activation following injury. Cell Stem Cell 23, 46–59.e5 (2018). [PubMed: 29887318]
6. Lee JC, Biasci D, Roberts R, Gearry RB, Mansfield JC, Ahmad T, Prescott NJ, Satsangi J, Wilson DC, Jostins L, Anderson CA; UK IBD Genetics Consortium, Traherne JA, Lyons PA, Parkes M, Smith KGC, Genome-wide association study identifies distinct genetic contributions to prognosis and susceptibility in Crohn's disease. Nat. Genet. 49, 262–268 (2017). [PubMed: 28067912]
7. Piovani D, Danese S, Peyrin-Biroulet L, Nikolopoulos GK, Lytras T, Bonovas S, Environmental risk factors for inflammatory bowel diseases: An umbrella review of meta-analyses. Gastroenterology 157, 647–659.e4 (2019). [PubMed: 31014995]
8. Fritz T, Niederreiter L, Adolph T, Blumberg RS, Kaser A, Crohn's disease: NOD2, autophagy and ER stress converge. Gut 60, 1580–1588 (2011). [PubMed: 21252204]
9. Cadwell K, Liu JY, Brown SL, Miyoshi H, Loh J, Lennerz JK, Kishi C, Kc W, Carrero JA, Hunt S, Stone CD, Brunt EM, Xavier RJ, Sleckman BP, Li E, Mizushima N, Stappenbeck TS, Virgin IV HW, A key role for autophagy and the autophagy gene Atg16l1 in mouse and human intestinal Paneth cells. Nature 456, 259–263 (2008). [PubMed: 18849966]
10. Cadwell K, Patel KK, Maloney NS, Liu TC, Ng ACY, Storer CE, Head RD, Xavier R, Stappenbeck TS, Virgin HW, Virus-plus-susceptibility gene interaction determines Crohn's disease gene Atg16L1 phenotypes in intestine. Cell 141, 1135–1145 (2010). [PubMed: 20602997]
11. Liu TC, Kern JT, VanDussen KL, Xiong S, Kaiko GE, Wilen CB, Rajala MW, Caruso R, Holtzman MJ, Gao F, McGovern DPB, Nunez G, Head RD, Stappenbeck TS, Interaction between smoking and ATG16L1T300A triggers Paneth cell defects in Crohn's disease. J. Clin. Invest. 128, 5110–5122 (2018). [PubMed: 30137026]
12. Liu TC, Gurram B, Baldridge MT, Head R, Lam V, Luo C, Cao Y, Simpson P, Hayward M, Holtz ML, Bousounis P, Noe J, Lerner D, Cabrera J, Biank V, Stephens M, Huttenhower C, McGovern

DPB, Xavier RJ, Stappenbeck TS, Salzman NH, Paneth cell defects in Crohn's disease promote dysbiosis. JCI Insight 1, e86907 (2016). [PubMed: 27699268]

13. Takagawa T, Kitani A, Fuss I, Levine B, Brant SR, Peter I, Tajima M, Nakamura S, Strober W, An increase in LRRK2 suppresses autophagy and enhances Dectin-1-induced immunity in a mouse model of colitis. Sci. Transl. Med. 10, eaan8162 (2018). [PubMed: 29875204]
14. Watanabe R, Buschauer R, Böhning J, Audagnotto M, Lasker K, Lu TW, Boassa D, Taylor S, Villa E, The in situ structure of Parkinson's disease-linked LRRK2. Cell 182, 1508–1518.e16 (2020). [PubMed: 32783917]
15. Usmani A, Shavarebi F, Hiniker A, The cell biology of LRRK2 in Parkinson's disease. Mol. Cell. Biol. 41, e00660–20 (2021). [PubMed: 33526455]
16. Derkinderen P, Neunlist M, Crohn's and Parkinson disease: Is LRRK2 lurking around the corner? Nat. Rev. Gastroenterol. Hepatol. 15, 330–331 (2018). [PubMed: 29666431]
17. Zhang Q, Pan Y, Yan R, Zeng B, Wang H, Zhang X, Li W, Wei H, Liu Z, Commensal bacteria direct selective cargo sorting to promote symbiosis. Nat. Immunol. 16, 918–926 (2015). [PubMed: 26237551]
18. Liu TC, Naito T, Liu Z, VanDussen KL, Haritunians T, Li D, Endo K, Kawai Y, Nagasaki M, Kinouchi Y, McGovern DP, Shimosegawa T, Kakuta Y, Stappenbeck TS, LRRK2 but not ATG16L1 is associated with Paneth cell defect in Japanese Crohn's disease patients. JCI Insight 2, e91917 (2017). [PubMed: 28352666]
19. Ahmadi Rastegar D, Dzamko N, Leucine rich repeat kinase 2 and innate immunity. Front. Neurosci. 14, 193 (2020). [PubMed: 32210756]
20. Matsuzawa-Ishimoto Y, Shono Y, Gomez LE, Hubbard-Lucey VM, Cammer M, Neil J, Dewan MZ, Lieberman SR, Lazrak A, Marinis JM, Beal A, Harris PA, Bertin J, Liu C, Ding Y, van den Brink MRM, Cadwell K, Autophagy protein ATG16L1 prevents necroptosis in the intestinal epithelium. J. Exp. Med. 214, 3687–3705 (2017). [PubMed: 29089374]
21. Araujo A, Safronova A, Burger E, López-Yglesias A, Giri S, Camanzo ET, Martin AT, Grivennikov S, Yarovinsky F, IFN-γ mediates Paneth cell death via suppression of mTOR. eLife 10, e60478 (2021). [PubMed: 34633285]
22. Xie Y, Zhao Y, Shi L, Li W, Chen K, Li M, Chen X, Zhang H, Li T, Matsuzawa-Ishimoto Y, Yao X, Shao D, Ke Z, Li J, Chen Y, Zhang X, Cui J, Cui S, Leng Q, Cadwell K, Li X, Wei H, Zhang H, Li H, Xiao H, Gut epithelial TSC1/mTOR controls RIPK3-dependent necroptosis in intestinal inflammation and cancer. J. Clin. Invest. 130, 2111–2128 (2020). [PubMed: 31961824]
23. Haber AL, Biton M, Rogel N, Herbst RH, Shekhar K, Smillie C, Burgin G, Delorey TM, Howitt MR, Katz Y, Tirosh I, Beyaz S, Dionne D, Zhang M, Raychowdhury R, Garrett WS, Rozenblatt-Rosen O, Shi HN, Yilmaz O, Xavier RJ, Regev A, A single-cell survey of the small intestinal epithelium. Nature 551, 333–339 (2017). [PubMed: 29144463]
24. Biton M, Haber AL, Rogel N, Burgin G, Beyaz S, Schnell A, Ashenberg O, Su C-W, Smillie C, Shekhar K, Chen Z, Wu C, Ordovas-Montanes J, Alvarez D, Herbst RH, Zhang M, Tirosh I, Dionne D, Nguyen LT, Xifaras ME, Shalek AK, von Andrian UH, Graham DB, Rozenblatt-Rosen O, Shi HN, Kuchroo V, Yilmaz OH, Regev A, Xavier RJ, T helper cell cytokines modulate intestinal stem cell renewal and differentiation. Cell 175, 1307–1320.e22 (2018). [PubMed: 30392957]
25. Balasubramanian I, Bandyopadhyay S, Flores J, Bianchi-Smak J, Lin X, Liu H, Sun S, Golovchenko NB, Liu Y, Wang D, Patel R, Joseph I, Suntornsaratoon P, Vargas J, Green PHR, Bhagat G, Lagana SM, Ying W, Zhang Y, Wang Z, Li WV, Singh S, Zhou Z, Kollias G, Farr LA, Moonah SN, Yu S, Wei Z, Bonder EM, Zhang L, Kiela PR, Edelblum KL, Ferraris R, Liu TC, Gao N, Infection and inflammation stimulate expansion of a $CD74^{+}$ Paneth cell subset to regulate disease progression. EMBO J. 42, e113975 (2023). [PubMed: 37718683]
26. Pelka K, Hofree M, Chen JH, Sarkizova S, Pirl JD, Jorgji V, Bejnood A, Dionne D, Ge WH, Xu KH, Chao SX, Zollinger DR, Lieb DJ, Reeves JW, Fuhrman CA, Hoang ML, Delorey T, Nguyen LT, Waldman J, Klapholz M, Wakiro I, Cohen O, Albers J, Smillie CS, Cuoco MS, Wu J, Su MJ, Yeung J, Vijaykumar B, Magnuson AM, Asinovski N, Moll T, Goder-Reiser MN, Applebaum AS, Brais LK, DelloStritto LK, Denning SL, Phillips ST, Hill EK, Meehan JK, Frederick DT, Sharova T, Kanodia A, Todres EZ, Jané-Valbuena J, Biton M, Izar B, Lambden CD, Clancy TE, Bleday R, Melnitchouk N, Irani J, Kunitake H, Berger DL, Srivastava A, Hornick JL, Ogino S,

Rotem A, Vigneau S, Johnson BE, Corcoran RB, Sharpe AH, Kuchroo VK, Ng K, Giannakis M, Nieman LT, Boland GM, Aguirre AJ, Anderson AC, Rozenblatt-Rosen O, Regev A, Hacohen N, Spatially organized multicellular immune hubs in human colorectal cancer. Cell 184, 4734–4752.e20 (2021). [PubMed: 34450029]

27. Dominguez Conde C, Xu C, Jarvis LB, Rainbow DB, Wells SB, Gomes T, Howlett SK, Suchanek O, Polanski K, King HW, Mamanova L, Huang N, Szabo PA, Richardson L, Bolt L, Fasouli ES, Mahbubani KT, Prete M, Tuck L, Richoz N, Tuong ZK, Campos L, Mousa HS, Needham EJ, Pritchard S, Li T, Elmentaite R, Park J, Rahmani E, Chen D, Menon DK, Bayraktar OA, James LK, Meyer KB, Yosef N, Clatworthy MR, Sims PA, Farber DL, Saeb-Parsy K, Jones JL, Teichmann SA, Cross-tissue immune cell analysis reveals tissue-specific features in humans. Science 376, eabl5197 (2022). [PubMed: 35549406]
28. Kelly K, Chang A, Hastings L, Abdelmotilib H, West AB, Genetic background influences LRRK2-mediated Rab phosphorylation in the rat brain. Brain Res. 1759, 147372 (2021). [PubMed: 33600829]
29. Franchi L, Eigenbrod T, Muñoz-Planillo R, Ozkurede U, Kim YG, Chakrabarti A, Gale M Jr., Silverman RH, Colonna M, Akira S, Núñez G, Cytosolic double-stranded RNA activates the NLRP3 inflammasome via MAVS-induced membrane permeabilization and K+ efflux. J. Immunol. 193, 4214–4222 (2014). [PubMed: 25225670]
30. Dikovskaya D, Pemberton R, Taylor M, Tasegian A, Zenevicuite K, Sammler EM, Howden AJM, Alessi DR, Swamy M, Regulation of leucine-rich repeat kinase 2 by inflammation and IL-4. bioRxiv 591170 [Preprint] (2024); 10.1101/2024.04.29.591170.
31. Dhekne HS, Tonelli F, Yeshaw WM, Chiang CY, Limouse C, Jaimon E, Purlyte E, Alessi DR, Pfeffer SR, Genome-wide screen reveals Rab12 GTPase as a critical activator of Parkinson's disease-linked LRRK2 kinase. eLife 12, e87098 (2023). [PubMed: 37874635]
32. Lassen KG, Kuballa P, Conway KL, Patel KK, Becker CE, Peloquin JM, Villablanca EJ, Norman JM, Liu TC, Heath RJ, Becker ML, Fagbami L, Horn H, Mercer J, Yilmaz OH, Jaffe JD, Shamji AF, Bhan AK, Carr SA, Daly MJ, Virgin HW, Schreiber SL, Stappenbeck TS, Xavier RJ, Atg16L1 T300A variant decreases selective autophagy resulting in altered cytokine signaling and decreased antibacterial defense. Proc. Natl. Acad. Sci. U.S.A. 111, 7741–7746 (2014). [PubMed: 24821797]
33. Liu Y, Hao C, Zhang W, Liu Y, Guo S, Li R, Peng M, Xu Y, Pei X, Yang H, Zhao Y, Leucine-rich repeat kinase-2 deficiency protected against cardiac remodelling in mice via regulating autophagy formation and degradation. J. Adv. Res. 37, 107–117 (2022). [PubMed: 35499056]
34. Rocchi A, Yamamoto S, Ting T, Fan Y, Sadleir K, Wang Y, Zhang W, Huang S, Levine B, Vassar R, He C, A Becn1 mutation mediates hyperactive autophagic sequestration of amyloid oligomers and improved cognition in Alzheimer's disease. PLOS Genet. 13, e1006962 (2017). [PubMed: 28806762]
35. Shoji-Kawata S, Sumpter R, Leveno M, Campbell GR, Zou Z, Kinch L, Wilkins AD, Sun Q, Pallauf K, MacDuff D, Huerta C, Virgin HW, Helms JB, Eerland R, Tooze SA, Xavier R, Lenschow DJ, Yamamoto A, King D, Lichtarge O, Grishin NV, Spector SA, Kaloyanova DV, Levine B, Identification of a candidate therapeutic autophagy-inducing peptide. Nature 494, 201–206 (2013). [PubMed: 23364696]
36. Kingwell K, LRRK2-targeted Parkinson disease drug advances into phase III. Nat. Rev. Drug Discov. 22, 3–5 (2023). [PubMed: 36509915]
37. Gao P, Liu H, Huang H, Sun Y, Jia B, Hou B, Zhou X, Strober W, Zhang F, The Crohn disease-associated ATG16L1(T300A) polymorphism regulates inflammatory responses by modulating TLR- and NLR-mediated signaling. Autophagy 18, 2561–2575 (2022). [PubMed: 35220902]
38. Lin CH, Lin HY, Ho EP, Ke YC, Cheng MF, Shiue CY, Wu CH, Liao PH, Hsu AYH, Chu LA, Liu YD, Lin YH, Tai YC, Shun CT, Chiu HM, Wu MS, Mild chronic colitis triggers parkinsonism in LRRK2 mutant mice through activating TNF-α pathway. Mov. Disord. 37, 745–757 (2022). [PubMed: 34918781]
39. Weindel CG, Martinez EL, Zhao X, Mabry CJ, Bell SL, Vail KJ, Coleman AK, VanPortfliet JJ, Zhao B, Wagner AR, Azam S, Scott HM, Li P, West AP, Karpac J, Patrick KL, Watson RO, Mitochondrial ROS promotes susceptibility to infection via gasdermin D-mediated necroptosis. Cell 185, 3214–3231.e23 (2022). [PubMed: 35907404]

40. Valavanidis A, Vlachogianni T, Fiotakis K, Tobacco smoke: Involvement of reactive oxygen species and stable free radicals in mechanisms of oxidative damage, carcinogenesis and synergistic effects with other respirable particles. Int. J. Environ. Res. Public Health 6, 445–462 (2009). [PubMed: 19440393]

41. Eguchi T, Sakurai M, Wang Y, Saito C, Yoshii G, Wileman T, Mizushima N, Kuwahara T, Iwatsubo T, The V-ATPase–ATG16L1 axis recruits LRRK2 to facilitate the lysosomal stress response. J. Cell Biol. 223, e202302067 (2024). [PubMed: 38227290]

42. Chen Y, Yang Z, Wang S, Ma Q, Li L, Wu X, Guo Q, Tao L, Shen X, Boosting ROS-mediated lysosomal membrane permeabilization for cancer ferroptosis therapy. Adv. Healthc. Mater. 12, e2202150 (2023). [PubMed: 36408929]

43. Rocha EM, de Miranda BR, Castro S, Drolet R, Hatcher NG, Yao L, Smith SM, Keeney MT, di Maio R, Kofler J, Hastings TG, Greenamyre JT, LRRK2 inhibition prevents endolysosomal deficits seen in human Parkinson's disease. Neurobiol. Dis. 134, 104626 (2020). [PubMed: 31618685]

44. Houtman J, Freitag K, Gimber N, Schmoranzer J, Heppner FL, Jendrach M, Beclin1-driven autophagy modulates the inflammatory response of microglia via NLRP3. EMBO J. 38, e99430 (2019). [PubMed: 30617086]

45. Liu TC, Kern JT, Jain U, Sonnek NM, Xiong S, Simpson KF, VanDussen KL, Winkler ES, Haritunians T, Malique A, Lu Q, Sasaki Y, Storer C, Diamond MS, Head RD, McGovern DPB, Stappenbeck TS, Western diet induces Paneth cell defects through microbiome alterations and farnesoid X receptor and type I interferon activation. Cell Host Microbe 29, 988–1001.e6 (2021). [PubMed: 34010595]

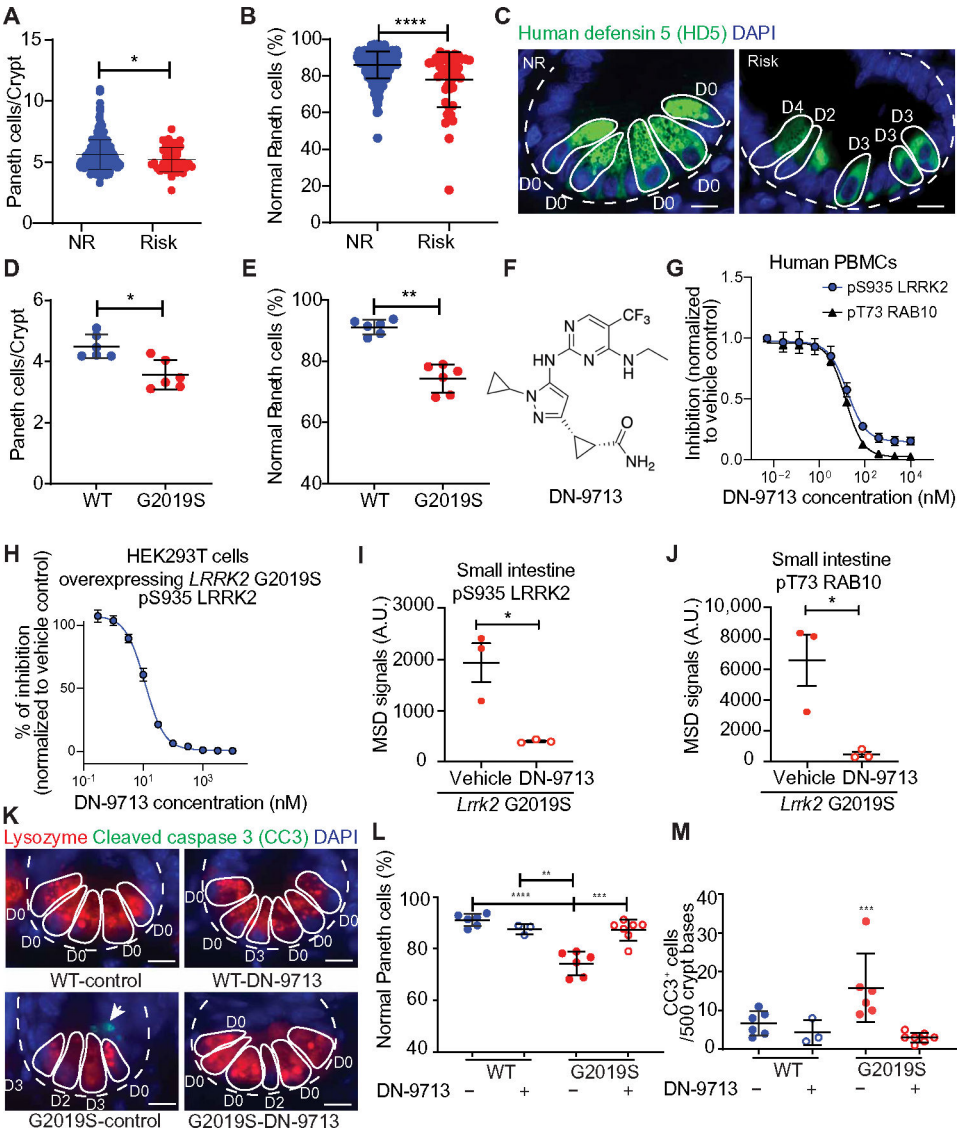

Fig. 1. Patients with CD harboring *LRRK2* SNPs and *Lrrk2* G2019S mice are prone to Paneth cell defects.

(**A**) Paneth cells per crypt and (**B**) percentages of normal Paneth cells in patients with CD carrying *LRRK2* risk alleles (N2081D and G2019S). (**C**) Representative photomicrographs of Paneth cells by defensin 5 (HD5, green); Blue: DAPI (4′,6-diamidino-2-phenylindole), nuclei. Scale bar, 10 μm. Paneth cells are outlined in white and classified into normal (D0) and five abnormal (D1 to D5) categories. (**D**) Ileal Paneth cells per crypt and (**E**) percentages of normal Paneth cells in *Lrrk2* G2019S mice ($n = 6$). (**F**) Structure of DN-9713, an LRRK2 kinase inhibitor. (**G**) Ex vivo treatment of healthy human PBMCs with DN-9713 on pS935 LRRK2 and pT73 RAB10 ($n = 3$ donors). Data are shown as mean ± SEM. Calculated mean unbound IC_{50} [95% confidence interval (CI)] for pS935 LRRK2, 10.8 nM (6.6 to 17.7 nM); for pT73 RAB10, 9.3 nM (6.8 to 12.6 nM). (**H**) Dose-response curves of LRRK2 inhibition by DN-9713 measured by pS935 LRRK2 in HEK293T cells overexpressing *LRRK2* G2019S. Data shown as mean ± SEM. $n = 8$ experiments. Mean of IC_{50} (95% CI):

11.5 nM (10 to 13 nM). (**I** and **J**) pS935 LRRK2 and pT73 RAB10 were measured by a Meso Scale Discovery (MSD) assay in the small intestines from *Lrrk2* G2019S mice with in-diet dosing of DN-9713 ($n = 3$). (**K**) Representative photomicrographs of Paneth cells with lysozyme (red) and CC3 (green and highlighted by arrow) from *Lrrk2* G2019S mice treated with DN-9713. Blue: DAPI. Scale bar, 10 μm. (**L**) Percentages of normal Paneth cells and (**M**) $CC3^+$ cells/500 crypts in *Lrrk2* G2019S mice treated with DN-9713 ($n = 3$ to 7). Statistical analysis by Mann-Whitney test [(A), (B), (D), and (E)], unpaired *t* test [(I) and (J)], or two-way ANOVA with Tukey's multicomparison test [(L) and (M)]. $*P < 0.05$; $**P < 0.01$; $***P < 0.001$; $****P < 0.0001$. Error bars represent SDs unless specially stated.

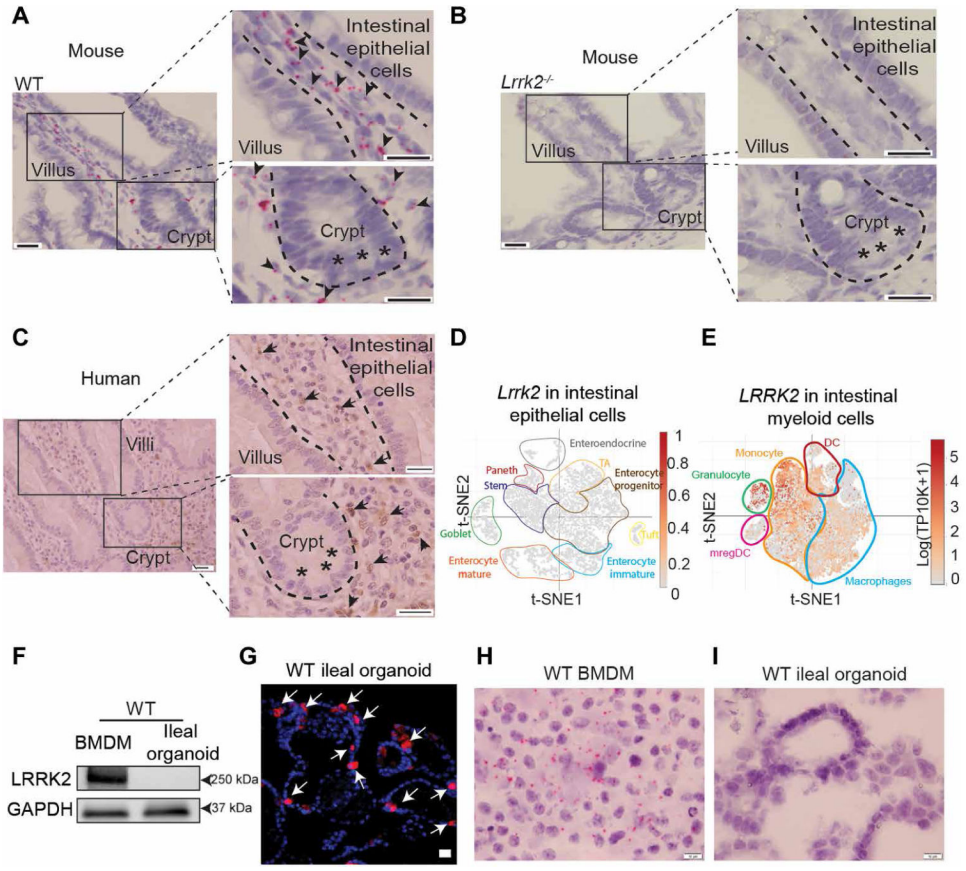

Fig. 2. *LRRK2* is detectable in lamina propria phagocytes but not intestinal epithelial cells.

Representative photomicrographs of in situ hybridization of *Lrrk2* in ilea from (**A**) WT and (**B**) *Lrrk2*$^{-/-}$ mice. Arrowheads represent *Lrrk2* RNA. Scale bars, 20 μm. (**C**) Representative photomicrographs of LRRK2 IHC in the ilea from patients with CD. Arrows represent LRRK2 protein. Scale bars, 20 μm. [(A) to (C)] The dashed lines represent the borders for intestinal epithelial cells, villi, and crypts in ileum. Asterisks represent Paneth cells. (**D**) Reanalysis of a previously generated scRNA-seq dataset (23) showed lack of *Lrrk2* expression in small intestinal epithelial cells. (**E**) Reanalysis of a previously generated human intestinal myeloid cell scRNA-seq dataset (26) showed robust *LRRK2* expression in monocytes and macrophages. (**F**) LRRK2 immunoblot in BMDMs and ileal organoids from WT mice. (**G**) Ileal organoids from WT mice used in (F) showed lysozyme expression by immunofluorescence (red/arrows). Blue: DAPI. Scale bars, 20 μm. Representative photomicrographs of in situ hybridization of *Lrrk2* in (**H**) BMDM and (**I**) ileal organoid from WT mice. Scale bars, 10 μm.

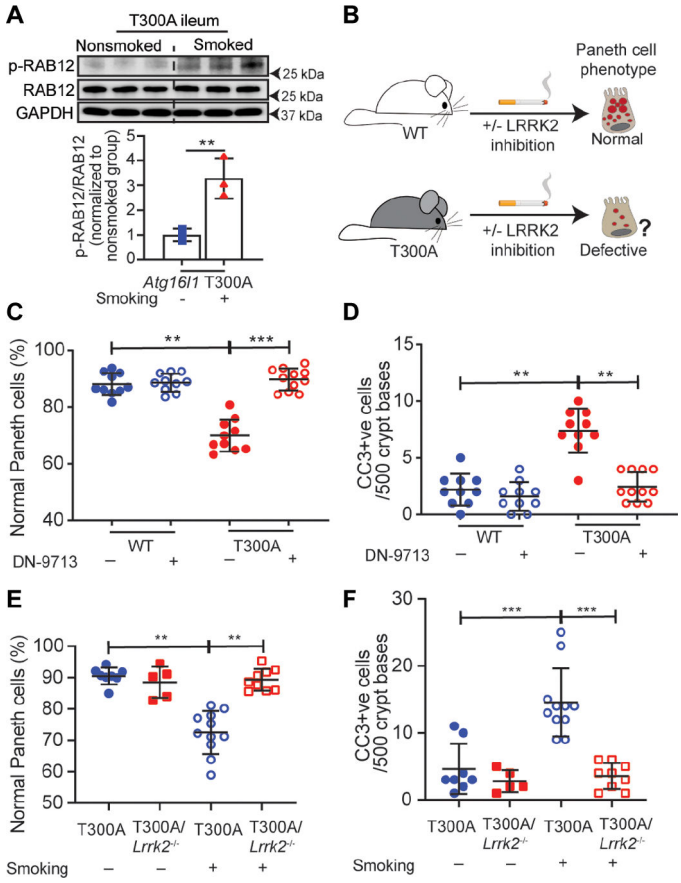

Fig. 3. LRRK2 inhibitor rescued Paneth cell defects in *Atg16l1* T300A smoke-exposed mice.

(**A**) Top: pS106 RAB12 immunoblot in ilea from *Atg16l1* T300A smoke-exposed and nonexposed mice. Bottom: Quantification of pS106 RAB12 expression ($n = 3$). (**B**) Schematic illustration of experimental design. *Atg16l1* T300A mice and littermates were exposed to cigarette smoke and treated with DN-9713. (**C**) Percentages of normal Paneth cells and (**D**) $CC3^+$ cells per 500 crypts from *Atg16l1* T300A smoke-exposed mice treated with DN-9713 ($n = 9$ to 11). (**E**) Percentages of normal Paneth cells and (**F**) crypt base $CC3^+$ cells per 500 crypts from *Atg16l1* T300A and *Atg16l1* T300A/*Lrrk2*$^{-/-}$ mice exposed to cigarette smoke ($n = 5$ to 11). Statistical analysis by unpaired *t* test (A) or two-way ANOVA followed with Tukey's multicomparison test [(C) to (F)]. $^{**}P < 0.01$; $^{***}P < 0.001$; $^{****}P < 0.0001$. Error bars represent SDs.

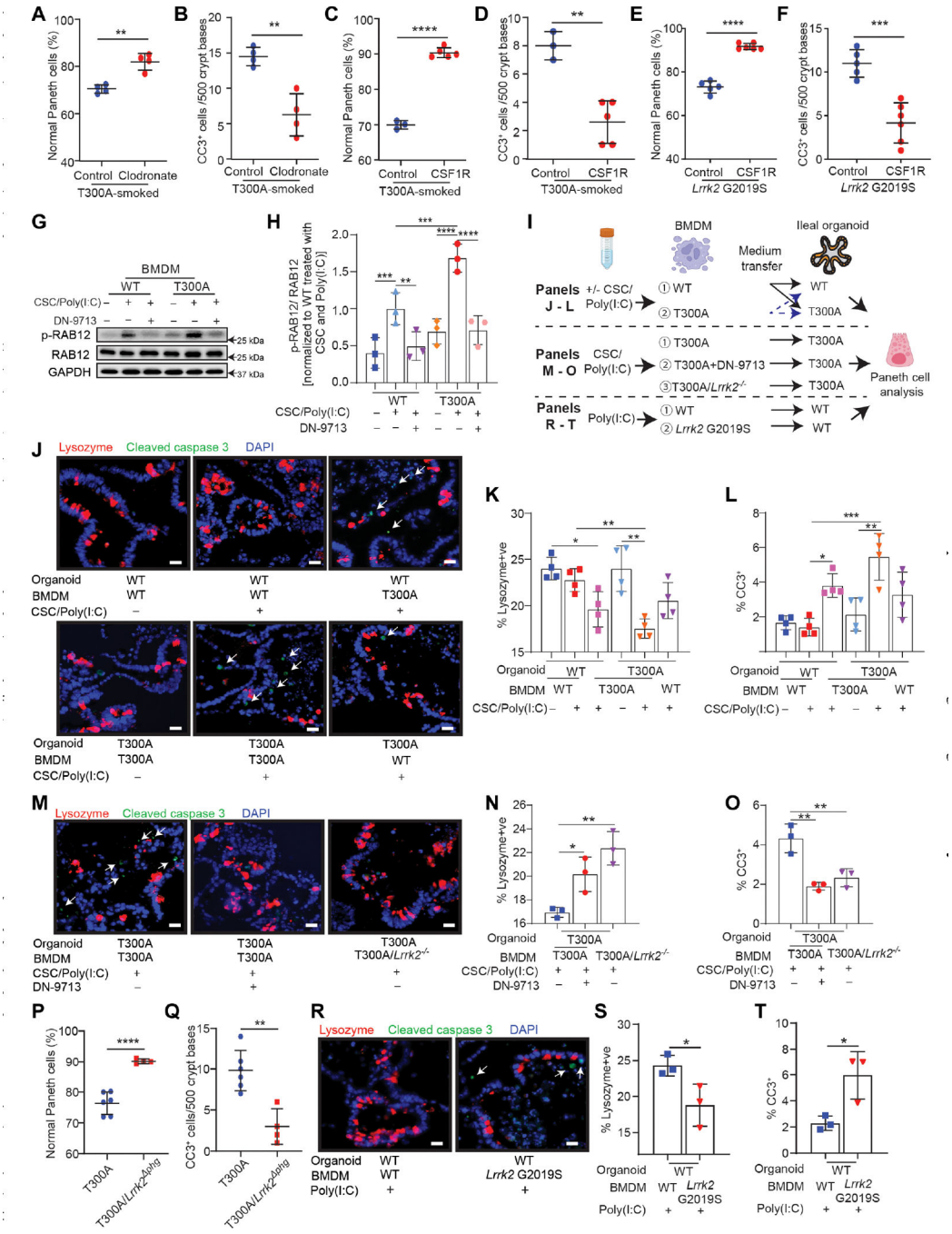

Fig. 4. *Atg16l1* T300A macrophages treated with cigarette smoke condensate induced Paneth cell defects in organoids.

(**A**, **C**, and **E**) Percentages of normal Paneth cells and (**B**, **D**, and **F**) $CC3^+$ cells per 500 crypts in the *Atg16l1* T300A smoke-exposed and *Lrrk2* G2019S mice treated with clodronate liposomes or anti-CSF1R antibody ($n = 3$ to 6). (**G**) pS106 RAB12 immunoblots in WT and *Atg16l1* T300A BMDMs treated with CSC/poly(I:C) ± DN-9713. (**H**) Quantification of pS106 RAB12 expression ($n = 3$). (**I**) Schematic illustration of experimental designs. (**J**) Representative immunofluorescence of lysozyme (red), CC3

(green and highlighted by arrows), and DAPI (blue) in organoids. Scale bars, 20 μm. Quantification of (**K**) Paneth cells and (**L**) $CC3^+$ cells in WT and *Atg16l1* T300A organoids with medium transferred from WT and *Atg16l1* T300A BMDMs. (**M**) Representative immunofluorescence of lysozyme (red), CC3 (green and highlighted by arrows), and DAPI (blue) in *Atg16l1* T300A organoids. Scale bars, 20 μm. Quantification of (**N**) Paneth cells and (**O**) $CC3^+$ cells in *Atg16l1* T300A organoids with medium transferred from *Atg16l1* T300A BMDMs treated with CSC/poly(I:C) ± DN-9713 or from *Atg16l1* T300A/*Lrrk2*$^{-/-}$ BMDMs treated with CSC/poly(I:C) ($n = 3$). (**P**) Percentages of normal Paneth cells and (**Q**) crypt base $CC3^+$ cells/500 crypts from *Atg16l1* T300A smoke-exposed and *Atg16l1* T300A/*Lrrk2*$^{\Delta phg}$ smoke-exposed mice ($n = 4$ to 6). (**R**) Representative immunofluorescence of lysozyme (red), CC3 (green and highlighted by arrows), and DAPI (blue) in WT organoids. Scale bars, 20 μm. Quantification of (**S**) Paneth cells and (**T**) $CC3^+$ cells in WT organoids with medium transferred from WT or *Lrrk2* G2019S BMDMs treated with poly(I:C) ($n = 3$). Statistical analysis by unpaired *t* test [(A) to (F), (P), (Q), (S), and (T)], two-way ANOVA [(H), (K),and (L)], or one-way ANOVA followed by Tukey's multicomparison test [(N) and (O)]. *$P < 0.05$; **$P < 0.01$; ***$P < 0.001$; ****$P < 0.0001$. Error bars represent SDs.

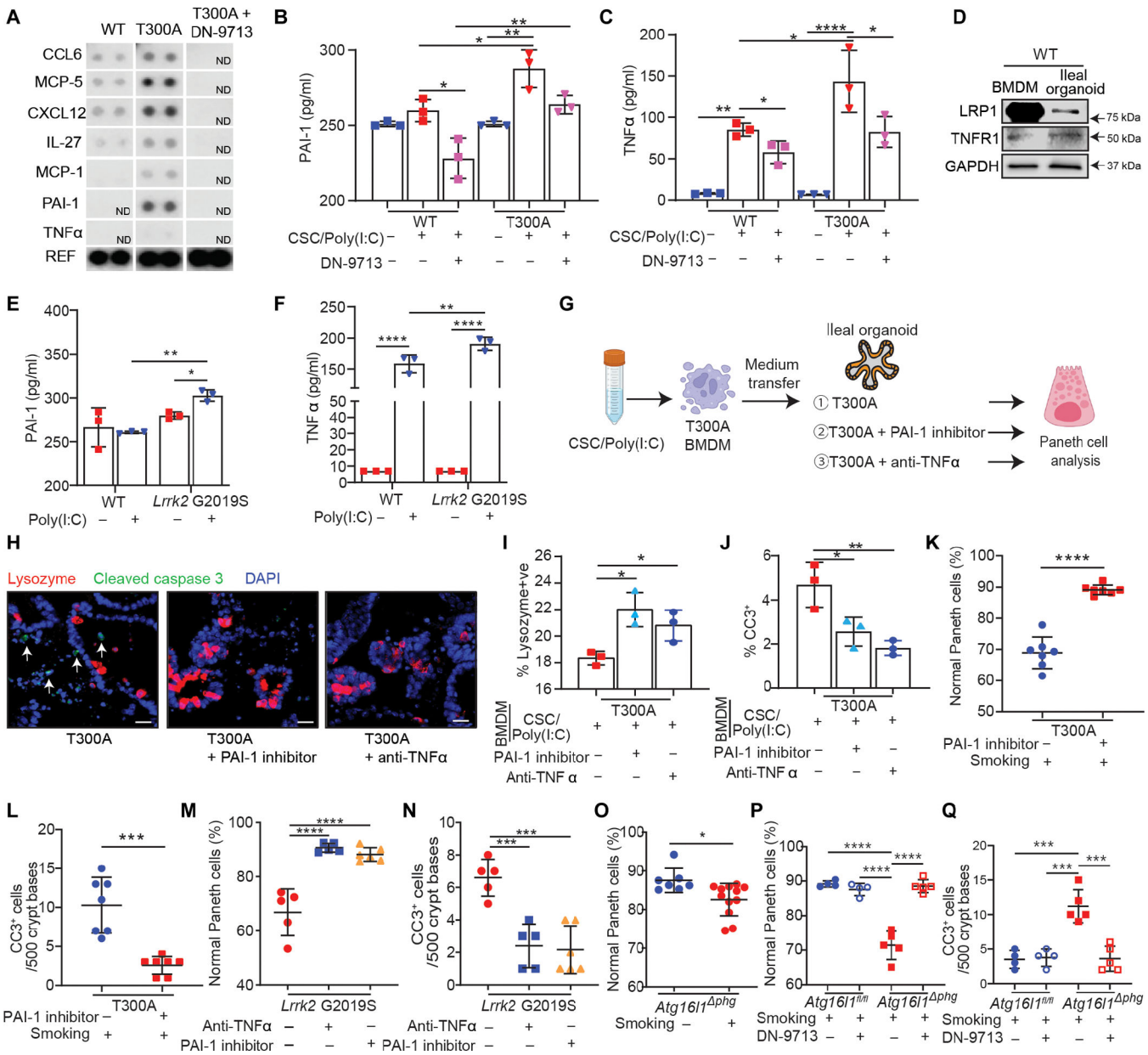

Fig. 5. TNF and PAI-1 are macrophage-secreted factors that induce Paneth cell defects.

(**A**) Detection of cytokines/chemokines produced from WT BMDMs treated with CSC/poly(I:C) and *Atg16l1* T300A BMDMs treated with CSC/poly(I:C) ± DN-9713. Concentrations of (**B**) PAI-1 and (**C**) TNF in BMDM medium ($n = 3$). (**D**) Protein expression of PAI-1 and TNF receptors LRP1 and TNFR1 by immunoblot in WT BMDMs and ileal organoids. Concentrations of (**E**) PAI-1 and (**F**) TNF by ELISA in medium from WT and *Lrrk2* G2019S BMDMs ($n = 3$). (**G**) Experimental scheme to define the roles of TNF and PAI-1 in mediating Paneth cell defects. (**H**) Representative immunofluorescence of lysozyme (red), CC3 (green and highlighted by arrows), and DAPI (blue) in *Atg16l1* T300A organoids. Scale bars, 20 μm. Quantification of (**I**) Paneth cells and (**J**) $CC3^+$ cells in *Atg16l1* T300A organoids with medium transferred from *Atg16l1* T300A BMDMs treated

with either PAI-1 inhibitor MDI-2268 or anti-TNF ($n = 3$). (**K**) Percentages of normal Paneth cells and (**L**) crypt base $CC3^+$ cells/500 crypts from *Atg16l1* T300A smoke-exposed mice treated with PAI-1 inhibitor ($n = 7$). (**M**) Percentages of normal Paneth cells and (**N**) crypt base $CC3^+$ cells/500 crypts from *Lrrk2* G2019S mice administrated with either PAI-1 inhibitor or anti-TNF ($n = 5$ or 6). (**O**) Percentages of normal Paneth cells in $Atg16l1^{\Delta phg}$ smoke-exposed mice ($n = 7$ to 12). (**P**) Percentages of normal Paneth cells and (**Q**) crypt base $CC3^+$ cells/500 crypts from $Atg16l1^{fl/fl}$ and $Atg16l1^{\Delta phg}$ smoke-exposed mice treated with DN-9713 ($n = 4$ or 5). Statistical analysis by two-way ANOVA followed by Tukey's multicomparison test [(B), (C), (E), (F), (P), and (Q)], one-way ANOVA followed by Tukey's multicomparison test [(I), (J), (M), and (N)], or unpaired *t* test [(K), (L), and (O)]. $*P < 0.05$; $**P < 0.01$; $***P < 0.001$; $****P < 0.0001$. Error bars represent SDs.

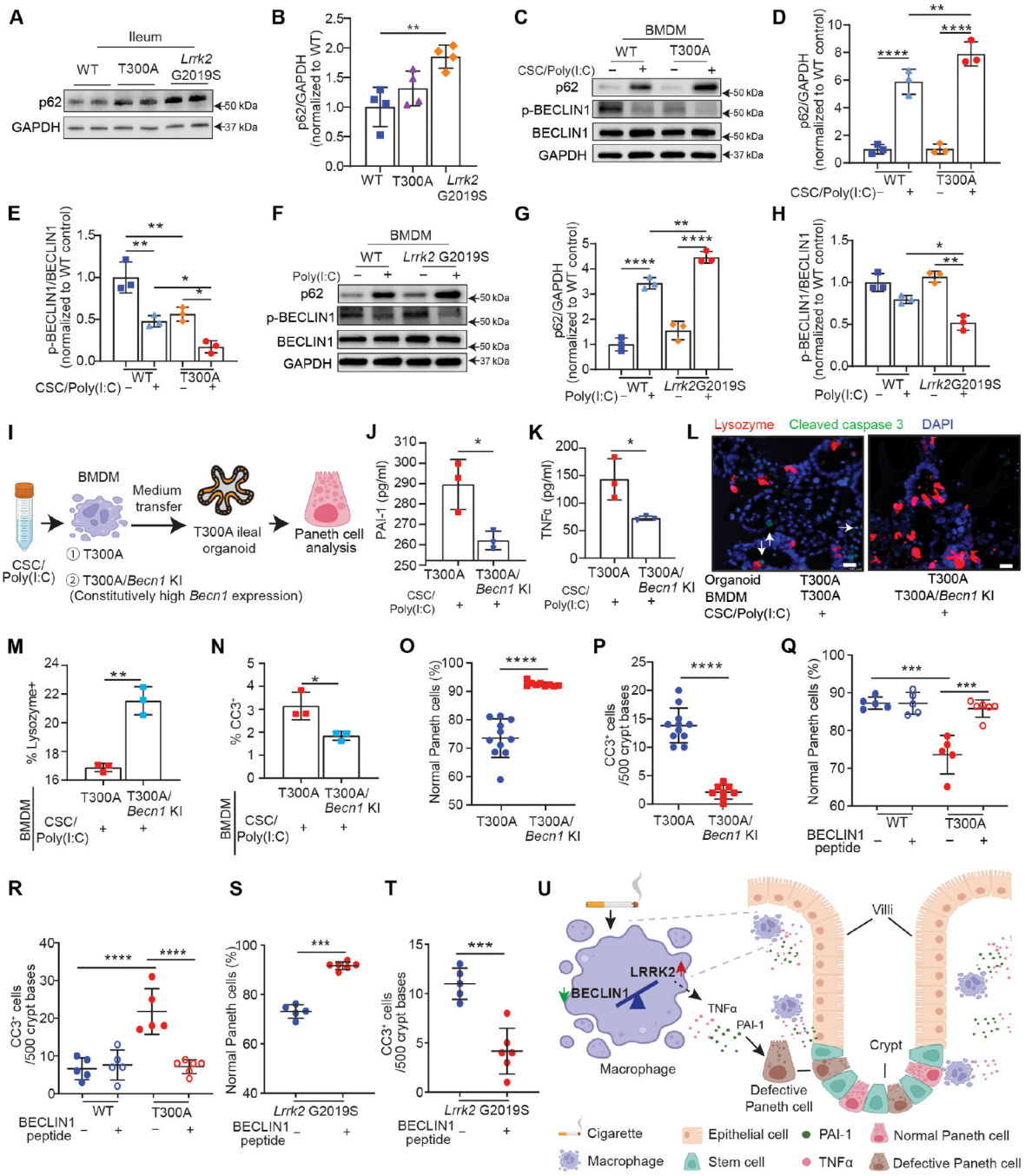

Fig. 6. Enforced Beclin1 activation prevents Paneth cell defects in *Atg16l1* T300A smoke-exposed and *Lrrk2* G2019S mice.

(**A**) p62 immunoblots in ilea from WT, *Atg16l1* T300A, and *Lrrk2* G2019S mice. (**B**) Quantification of p62 expression ($n = 4$). (**C**) p62 and pS15 Beclin1 immunoblots in WT and *Atg16l1* T300A BMDMs treated with CSC/poly(I:C). Quantification of (**D**) p62 and (**E**) pS15 Beclin1 expression ($n = 3$). (**F**) p62 and pS15 Beclin1 immunoblots in WT and *Lrrk2* G2019S BMDMs treated with poly(I:C). Quantification of (**G**) p62 and (**H**) pS15 Beclin1 expression ($n = 3$). (**I**) Experimental scheme involving BMDM medium transfer

to organoid culture. Concentrations of (**J**) PAI-1 and (**K**) TNF in BMDM medium (n = 3). (**L**) Representative immunofluorescence of lysozyme (red), CC3 (green and highlighted by arrows), and DAPI (blue) in *Atg16l1* T300A organoids with medium transferred from *Atg16l1* T300A or *Atg16l1* T300A/*Becn1* KI BMDMs. Scale bar, 20 μm. Quantification of (**M**) Paneth cells and (**N**) $CC3^+$ cells in *Atg16l1* T300A organoids (n = 3). (**O**) Percentages of normal Paneth cells and (**P**) crypt base $CC3^+$ cells/500 crypts in smoke-exposed mice (n = 9 to 11). (**Q**) Percentages of normal Paneth cells and (**R**) crypt base $CC3^+$ cells/500 crypts from WT and *Atg16l1* T300A smoke-exposed mice treated with Tat-Beclin1 peptide (n = 5 or 6). (**S**) Percentages of normal Paneth cells and (**T**) crypt base $CC3^+$ cells/500 crypts from *Lrrk2* G2019S mice treated with Tat-Beclin1 peptide (n = 5 or 6). (**U**) Current working model of how genetic factors or gene-environmental interactions trigger Paneth cell defects. Statistical analysis by one-way ANOVA followed by Tukey's multicomparison test (B), two-way ANOVA followed by Tukey's multicomparison test [(D), (E), (G), (H), (Q), and (R)], or unpaired t test [(J), (K), (M) to (P), (S), and (T)]. *P < 0.05; **P < 0.01; ***P < 0.001; ****P < 0.0001. Error bars represent SDs.